Journal of Metals, Materials and Minerals, Vol. 32, No. 1, pp. 55-64, 2022

Effect of pre-carbonization temperature on the porous structure and electrochemical properties of activated carbon fibers derived from kapok for supercapacitor applications

Nu Myat THAZIN[1,2], Nattapat CHAIAMMART[1,3], Myo Myo THU[1,2], and Gasidit PANOMSUWAN[1,2,3,*]

[1] *Department of Materials Engineering, Faculty of Engineering, Kasetsart University, Bangkok 10900, Thailand*
[2] *International Collaborative Education Program for Materials Technology, Education, and Research (ICE-Matter), ASEAN University Network, Southeast Asia Engineering Education Development Network (AUN/SEED-Net), Bangkok, Thailand*
[3] *Special Research Unit for Biomass Conversion Technology for Energy and Environmental Materials, Kasetsart University, Bangkok, Thailand*

***Corresponding author e-mail:** gasidit.p@ku.ac.th

Received date:
9 August 2021
Revised date
14 January 2022
Accepted date:
28 January 2022

Keywords:
Activated carbon fibers;
Kapok;
Pre-carbonization;
Chemical activation;
Supercapacitors

Abstract

Activated carbon fibers (ACFs) were successfully synthesized from kapok via a two-step process: (i) pre-carbonization and (ii) chemical activation. The pre-carbonization temperature was varied at 300°C, 400°C, and 500°C. The mixing ratio of the pre-carbonized product and potassium hydroxide (KOH) was 3:1, while the activation temperature was 800°C. The effect of pre-carbonization temperature on the morphology, surface area and porosity, chemical functional group, and phase structure of ACFs was investigated and discussed. The characterization results showed that ACFs exhibited an amorphous carbon structure with a hollow fiber shape resembling the kapok. The specific surface area decreased from 487 $m^2 \cdot g^{-1}$ to 326 $m^2 \cdot g^{-1}$ as the pre-carbonization increased. The pore structure of ACFs possessed a major contribution of micropores, and mesopores became more dominant at a high pre-carbonization temperature. The potential use of ACFs as electrode materials in supercapacitors was electrochemically tested by cyclic voltammetry and galvanostatic charge-discharge measurements. The ACFs obtained from pre-carbonization at 500°C had the highest specific capacitance of 31.9 $F \cdot g^{-1}$ at a current density of 1 $A \cdot g^{-1}$. The results in this work will be a helpful guideline for the further design and development of ACFs from kapok for supercapacitor applications.

1. Introduction

With the increase in the world's population, worldwide energy consumption has been growing at a steady rate. It was, as a matter of fact, estimated to be around 144,000 TWh in 2018. The most common energies come from fossil fuel, nuclear, and renewable sources (e.g., hydropower, wind, solar, geothermal, and biomass energy) [1]. In 1994, researchers found out that 90% of energy was not renewable, and the interest in renewable sources has grown significantly since then. However, the energy flow from these primary sources is not stable, and they rely heavily on weather conditions, seasons, and time of day [2]. Therefore, deploying qualified energy storage devices is required as an intermediate step before distribution to consumers. Among many types of energy storage devices, supercapacitors have been gaining attention because of their high charge-discharge rate, high power density, long life cycle, and eco-friendly nature [3,4]. Much more energy can be stored in supercapacitors when compared to traditional capacitors while possessing a higher power density than batteries. These benefits allow them to be used for backing up power in electronic devices, accelerating the engine starter in hybrid vehicles, and storing electricity generated from solar or wind energy [5].

Supercapacitors can be categorized into three types: (i) electric double-layer capacitor (EDLC), (ii) pseudo-capacitor, and (iii) hybrid capacitor [3-5]. Every type has a unique storage system: For instance, the storage system in an EDLC involves a non-faradaic or electrostatic process, in which charges are not stored by a chemical mechanism; in fact, charges are distributed on the electrode surface by a physical mechanism [6]. In the case of a pseudo-capacitor, a faradaic or electrochemical process takes place, in which the redox process occurs on the electrode [7]. A hybrid capacitor, on the other hand, consists of one electrode from the EDLC and another from the pseudo-capacitor, working together [8]. Both hybrid and pseudo-capacitors exhibit high capacitance and poor or moderate cycling stability, which can work as a disadvantage in real-life applications. Even though the EDLC does not possess high capacitance, it acquires moderate capacitance and excellent cycling stability [3-8].

The type of electrode material used is one of the vital factors that determines the performance and reliability of supercapacitors. In recent times, biomass-derived porous carbons, through the physical or chemical activation process, have proved to function as promising electrode materials for supercapacitors because of their high surface area, low cost, abundant and renewable sources, outstanding electrochemical

DOI: 10.55713/jmmm.v32i1.1247

performance [9-11]. Among several types of activated carbons, the activated carbon fibers (ACFs) derived from natural biomass fibers (e.g., silk [12], cotton [13,14], cattail wool [15], sisal [16], kapok [17,18], and banana fiber [19]) have come to occupy a place among of the promising electrode materials for supercapacitor applications, owing to their large surface area and high porosity, which can facilitate ion adsorption/desorption processes. Moreover, ACFs have lighter weight and are more flexible than commonly activated carbon powders. These advantages give rise to higher specific capacitance and are beneficial for fabricating flexible supercapacitor electrodes [11,16,20]. The surface area and type of porosity of ACFs play an essential role in controlling and enhancing capacitance in supercapacitors. Micropores (< 2 nm) provide the adsorption sites for electrolyte ions [21], while mesopores (2 nm to 50 nm) and macropores (>50 nm) serve as a transport path for fast electrolyte supply [22,23]. Based on several successful works on ACFs, the surface area and porous structure of ACFs were found to be varied broadly, depending on many factors, including the activation process [12], activator concentration [14,15], activation temperature [16], activation time [17], type of activator [19], and type of biomass [24]. Despite significant progress on ACFs, the pre-carbonization temperature is the factor that has been ignored and rarely been investigated by most studies on ACFs. Therefore, due to the lack of research in this regard in existing literature, it is highly desirable to investigate this factor to broaden the database and serve as a helpful reference for the rational design of ACFs with desirable surface area and pore structure.

In this work, ACFs were prepared from natural kapok fibers in a two-step process: (i) pre-carbonization and (ii) chemical activation. The pre-carbonization temperature was varied at 300°C, 400°C, and 500°C for 2 h under argon flow. After that, pre-carbonized samples were mixed with potassium hydroxide (KOH) as an activator and then activated at 800°C under argon flow. The effect of the pre-carbonization temperature on the chemical functionality, morphology, phase structure, and surface area and porosity of ACFs was investigated with Fourier transform infrared spectroscopy (FTIR), scanning electron microscopy (SEM), X-ray diffraction (XRD), and physical gas adsorption. Furthermore, the electrochemical measurements were taken from ACFs using a three-electrode system by cyclic voltammetry (CV) and galvanostatic charge-discharge (GCD) in an acidic solution to evaluate their potential use as electrode materials for the storage of the charges in the supercapacitor.

2. Experiment

2.1 Materials

Natural kapok (*Ceiba pentandra*) was obtained from the Chiang Rai province. Hydrochloric acid (HCl, 37%), isopropanol (C_3H_8O, purity 99.8%), potassium hydroxide (KOH, 85%), and sulfuric acid (H_2SO_4, 98%) were purchased from RCI Labscan Ltd. The Nafion® DE 521 solution (5 wt% in a mixture of lower aliphatic alcohols and water) was obtained from Sigma-Aldrich. Further, ultrapure water (18.2 MΩ·cm^{-1} at 25°C) was obtained from a Direct-Q™ 5 UV Millipore water purification system. All chemicals utilized in this work were of analytical grade and used without purification.

2.2 Preparation of pre-carbonized fibers (PCFs) from kapok

The kapok was first washed with tap water twice and then dried at 80°C for 24 h in an oven (Memmert, UN55). Four grams of dried kapok was loaded in a ceramic boat and then subjected to temperatures of 300°C, 400°C, and 500°C for 2 h with a heating rate of 10°C·min^{-1} under a gentle flow of Ar gas (0.2 L·min^{-1}) in a tube furnace (Vecstar, TFV1100) for pre-carbonization. The pre-carbonized fibers at 300°C, 400°C, and 500°C were designated as PCF-300, PCF-400, and PCF-500, respectively.

2.3 Preparation of activated carbon fibers (ACFs) from kapok

Three grams of each PCF was mixed with 1 g of KOH (PCF:KOH = 3:1) and then dispersed in 50 mL of deionized water. The mixture was vigorously stirred for 1 h at room temperature to obtain a homogeneous mixture. Afterwards, it was dried in an oven at 105°C for 24 h. The activation process was subsequently carried out in a tube furnace at 800°C for 1 h with a heating rate of 10°C·min^{-1} and naturally cooled to room temperature under a gentle flow of Ar gas (0.2 L·min^{-1}). The activated products were taken out and repeatedly washed with 1 M HCl solution and deionized water until a neutral pH was obtained. The products were finally dried at 105°C for 24 h to obtain ACFs. The ACFs prepared from PCF-300, PCF-400, and PCF-500 were designated as ACF-300, ACF-400, ACF-500, respectively. Figure 1 depicts the overall preparation process of the ACFs derived from kapok in this work.

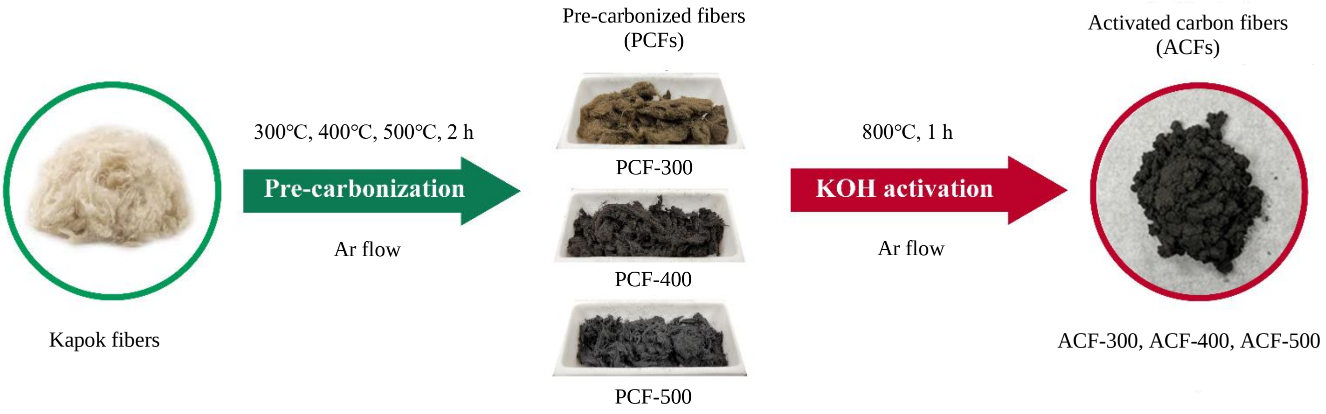

Figure 1. Schematic illustration for the overall preparation process of ACFs from kapok.

2.4 Characterizations

Morphology of the samples was investigated using a JEOL JSM-7600F field-emission scanning electron microscope at an acceleration voltage of 1 kV. The elemental composition of ACFs was evaluated on an AZtecOne energy dispersive spectroscopy (EDS) system from Oxford Instruments equipped with a Hitachi SU3500 scanning electron microscope at an acceleration voltage of 15 kV. The FTIR analysis was conducted on a Bruker Alpha-E spectrometer in the wavenumber range of 500 cm^{-1} to 4000 cm^{-1} to investigate the chemical functional groups. The phase structure of ACFs was examined with a Philips X'Pert X-ray diffractometer with Cu Kα radiation (λ = 0.154 nm), which was operated at 40 kV and 30 mA in the 2θ range between 5° and 70°. Nitrogen (N_2) adsorption-desorption isotherms were recorded at -196°C using a Micromeritics 3Flex surface characterization analyzer to investigate the specific surface area and pore-size distribution of ACFs. Before measurement, the ACFs were degassed using a Smart VacPrep at 200°C for 12 h under vacuum.

2.5 Electrochemical measurements

For the working electrode preparation, 5.0 mg of ACFs was dispersed in the mixture of 475 µL ultrapure water, 475 µL isopropanol, and 50 µL Nafion® DE 521. The mixture was sonicated for 1 h until homogeneous suspension was obtained. Following this, 3 µL of suspension was drop-casted onto a glassy carbon disk (3 mm disk diameter, ALS Co., Ltd.) and left in an ambient air condition until it was completely dried.

Electrochemical measurements were performed using a three-electrode system in a N_2-saturated 1 M H_2SO_4 solution at room temperature. A platinum wire (ALS Co., Ltd.) and Ag/AgCl in saturated KCl solution (ALS Co., Ltd.) were used as the counter electrode and reference electrode, respectively. Further, an ACF-modified glassy carbon electrode was used as the working electrode. Three electrodes were connected to a Biologic VSP potentiostat controlled by the EC-Lab software. The CV measurement was performed in the potential range of 0 V to 1 V at different scan rates from 10 mV·s^{-1} to 100 mV·s^{-1}. The CV curves were scanned until a stable curve was obtained. Then, the GCD measurement was conducted in the potential window of 0 V to 1 V at different current densities ranging from 1 A·g^{-1} to 20 A·g^{-1}. The stability test was examined by charging and discharging for 1500 cycles at the current density of 5 A·g^{-1}.

3. Results and discussion

3.1 Yields of PCFs and ACFs

After pre-carbonization, the yield of PCF-300, PCF-400, and PCF-500 was about 33%, 26%, and 12%, respectively, as compared to the starting raw kapok. A significant loss of weight at a high pre-carbonization temperature indicates more decomposition of the lignocellulosic structure of kapok. Generally, the hemicellulose started to decompose at about 220°C to 315°C, which is lower than the temperature for the decomposition of the cellulose (300°C to 400°C); it is also noted that lignin decomposed over a broad temperature range of 150°C to 900°C [25,26]. Therefore, the cellulose, hemicellulose, and lignin should remain in PCF-300, while a partial decomposition of cellulose and hemicellulose took place on PCF-400 and PCF-500, leaving lignin as the main component. In addition, the color of the PCFs also changed from brown (PCF-300) and dark brown (PCF-400) to black (PCF-500) as the pre-carbonization temperature increased, as shown in Figure 1. After activation, the ACFs revealed their black color with a fluffy feature regardless of the pre-carbonization temperature. The black color of PCFs implies the transformation of kapok into carbon materials. With the increasing pre-carbonization temperature, the yield of ACFs increased from 51% to 71% as compared to the weight of PCFs before activation.

3.2 Chemical functional groups

FTIR analysis was performed to examine the chemical functional groups of PCFs and ACFs. Figure 2 shows FTIR spectra of PCFs and ACFs. First, considering the PCF-300, a weak broad peak at 3364 cm^{-1} corresponded to the O–H stretching of the hydroxyl group [27]. The small peaks at around 2923 cm^{-1} and 2851 cm^{-1} were attributed to the C–H stretching in methyl and methylene groups [18]. The peak at 1694 cm^{-1} corresponded to the C=O stretching, while those at 1597 cm^{-1}, 1511 cm^{-1}, and 1439 cm^{-1} could be assigned to the C–C stretching in the different aromatic rings of lignin [28]. The absorption bands at 1000 cm^{-1} and 1300 cm^{-1} were associated with the C–O stretching in the ester group [24]. Compared to PCF-300, the C=O peaks became suppressed for PCF-400 and PCF-500, indicating the decomposition of cellulose and hemicellulose (decarboxylation) [29]. Additionally, the small bands at 875 cm^{-1}, 816 cm^{-1}, and 754 cm^{-1} of the out-of-plane C–H bending and stretching of the benzene rings were prominent for PCF-500 [30].

This result again confirms that cellulose, hemicellulose and lignin still remained in PCF-300, while lignin was the main component in PCF-400 and PCF-500 due to the decomposition of cellulose and hemicellulose. Such a difference in cellulose, hemicellulose and lignin components or chemical functional groups of the PCFs could lead to the different porosity development of ACFs during KOH activation [31-33]. In contrast to the PCFs, the FTIR spectra of ACFs had a similar

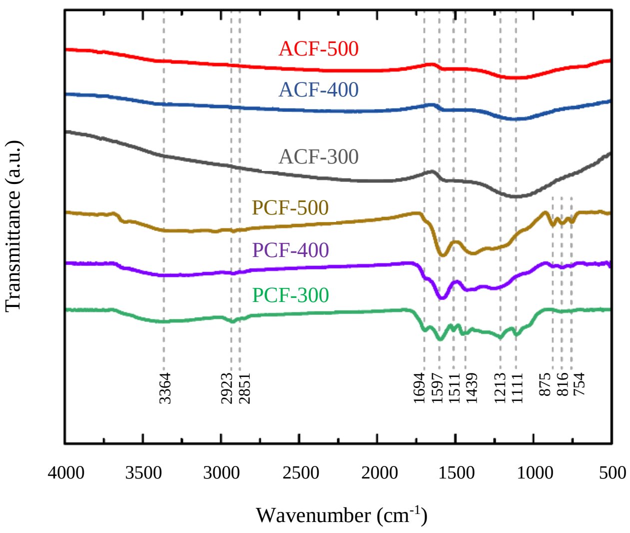

Figure 2. FTIR spectra of PCFs and ACFs.

feature with the near absence of functional groups, implying similar chemical properties and high carbon content. All absorption peaks vanished after KOH activation at high temperatures due to the destruction of the lignocellulosic structure remaining in PCFs.

3.3 Morphology

The SEM images of PCFs and ACFs are shown in Figure 3. Both PCFs and ACFs revealed a fiber shape with a diameter of about 20 μm to 30 μm, which was similar to that of the raw kapok. There was no noticeable change in morphology among the PCFs and ACFs with the changing pre-carbonization temperature, except some slight damage in the fiber structure of ACF-300. The EDS mapping images were also taken for all ACFs. The ACFs were composed of only C and O elements without impurities (Figure 4). The C and O contents estimated from the EDS spectra of all ACFs were about 88 at% and 12 at%, respectively. The FTIR and EDS results might suggest that the pre-carbonization temperature had no significant influence on the number of oxygen functionalities on ACFs.

3.4 Phase structure

The XRD patterns of ACFs are displayed in Figure 5. A prominent broad peak at 23° and a weak broad peak at 44° were clearly observed, which can be assigned to the (002) and (101) planes of the carbon phase, respectively [14,16]. These two visible peaks were evidence that all ACFs exhibited an amorphous carbon structure. No detection of other diffraction peaks confirmed that ACFs had high carbon purity. Moreover, the 2θ angle and shape of the diffraction peaks of ACF-300, ACF-400, and ACF-500 were almost similar, implying that the pre-carbonization temperature had no effect in altering the structural properties of ACFs.

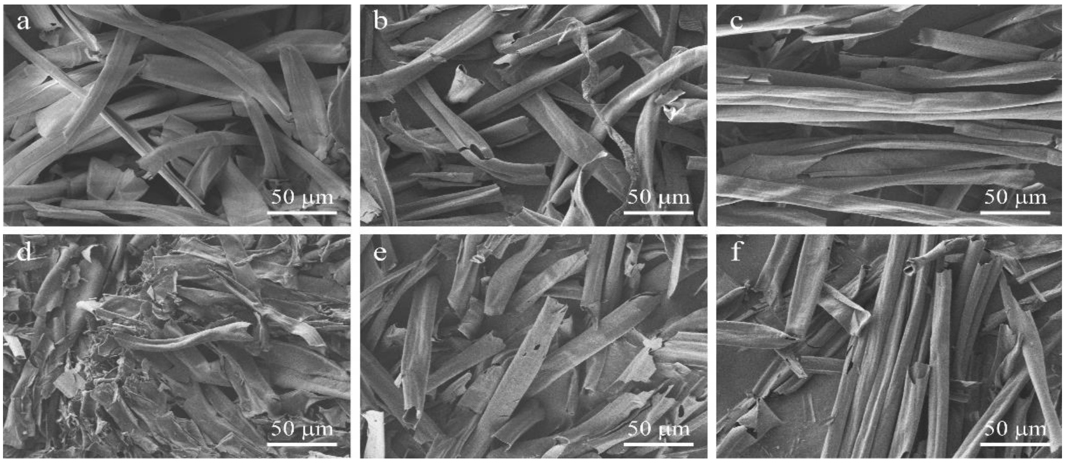

Figure 3. SEM images at a magnification of 500× for (a) PCF-300, (b) PCF-400, (c) PCF-500, (d) ACF-300, (e) ACF-400, and (f) ACF-500.

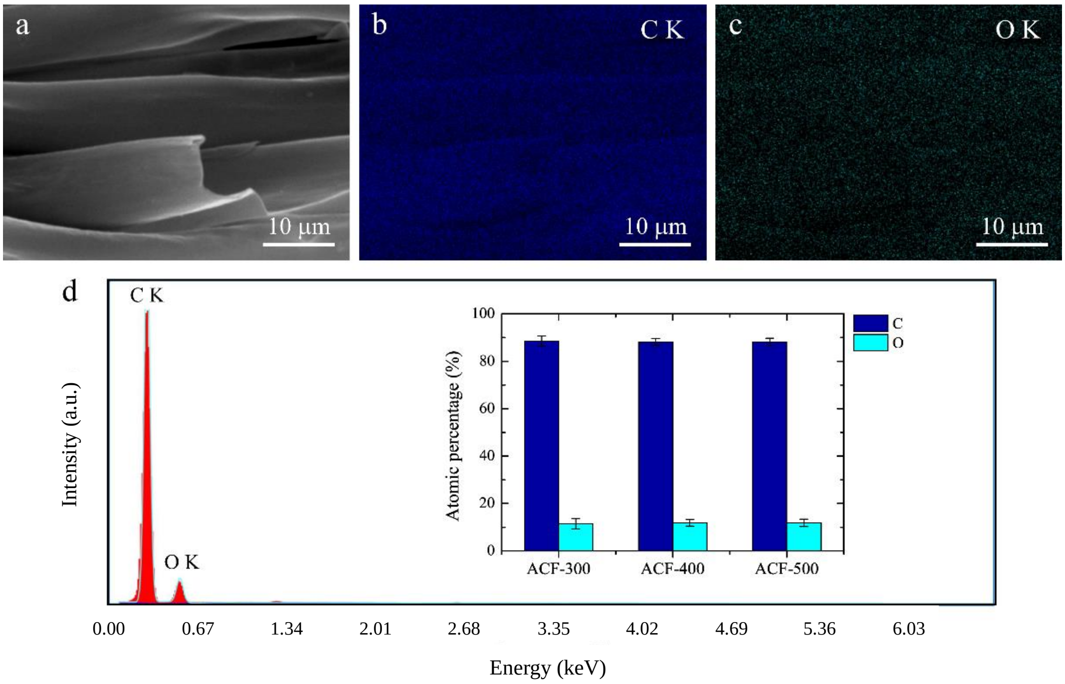

Figure 4. EDS mapping analysis of representative ACF-500: (a) SEM image, (b) C K signal, (c) O K signal, and (d) EDS spectrum (the inset shows the C and O contents averaged from five scan areas of ACF-300, ACF-400, and ACF-500).

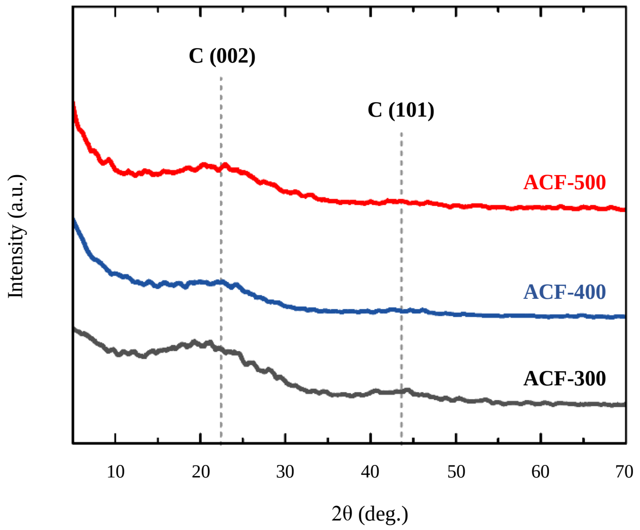

Figure 5. XRD patterns of ACF-300, ACF-400, and ACF-500.

3.5 Surface area and porosity analyses

Figure 6(a) shows the N_2 adsorption-desorption isotherms of ACFs. All isotherms showed a high N_2 quantity adsorbed at a low relative pressure (P/P_0) of 0.01 to 0.1. This isotherm characteristic corresponded to a type I isotherm according to the classification of International Union of Pure and Applied Chemistry (IUPAC), which affirms the significant contribution of micropores [34,35]. An almost-closed isotherm was observed for ACF-300; however, an unclosed isotherm was evident for ACF-400 and ACF-500. Such an unclosed isotherm can be explained by the following possible reasons: (i) Adsorption or pore-filling during the adsorption process caused the deformation of the non-rigid structure of ACFs (flexible pore structure due to its fluffy feature). (ii) Trapped nitrogen could not be released because of its affinity for the heterogeneous surface of ACFs. (iii) The near-solid state condensation of the adsorbate occurred at the entryway of pores [36,37]. The specific surface area of ACFs was calculated using the Brunauer-Emmett-Teller (BET) method utilizing the adsorption data in the P/P_0 range of 0.05 to 0.30. The BET specific surface area (S_{BET}) was found to decrease with the increasing pre-carbonization temperature: ACF-300 (487 $m^2 \cdot g^{-1}$) > ACF-400 (334 $m^2 \cdot g^{-1}$) > ACF-500 (326 $m^2 \cdot g^{-1}$). The density functional theory (DFT) model was further used to evaluate the pore-size distribution of ACFs, as shown in Figure 6(b). The ACF-300 had a narrow pore-size distribution at the micropore region (1.74 nm). However, for ACF-400 and ACF-500, it revealed a bimodal pore-size distribution consisting of a sharp peak of micropore at 1.61 nm and a broad peak of mesopore at about 3 nm.

The micropore specific surface area (S_{micro}) and micropore volume (V_{micro}) of the ACFs were obtained using the *t*-plot analysis. Based on isotherm characteristics and DFT pore-size distribution, it was assumed that the external specific surface area from the *t*-plot was only contributed by mesopores due to the lack of macropores ($S_{\mathrm{meso}} \approx S_{\mathrm{ext}} \approx S_{\mathrm{BET}} - S_{\mathrm{micro}}$). Thus, the specific surface area of ACFs was predominantly occupied by micropores (80% to 85%) while mesopores were a minor contribution (15% to 20%). The mesopore/micropore ratios (i.e., $S_{\mathrm{meso}}/S_{\mathrm{micro}}$ and $V_{\mathrm{meso}}/V_{\mathrm{micro}}$) were higher at a high pre-carbonization temperature, indicating a higher presence of mesopores in the ACFs. All textural parameters discussed above are summarized in Table 1. These results confirm that the pre-carbonization temperature before KOH activation plays an essential role in tailoring the micropores and mesopores of ACFs. The difference in the pore structure of ACFs prepared at different pre-carbonization temperatures is likely attributed to the different amounts of cellulose, hemicellulose, and lignin that remained in the PCFs. The presence of oxygen-containing functional groups (i.e., C–O and C=O) in cellulose and hemicellulose of PCF-300 could provide micropores during the activation of ACF-300. On the other hand, PCF-400 and PCF-500 were mainly composed of lignin with a small amount of cellulose and hemicellulose. Plentiful aromatic units in the lignin structure are chemically inert, thus producing mesopores in ACF-400 and ACF-500.

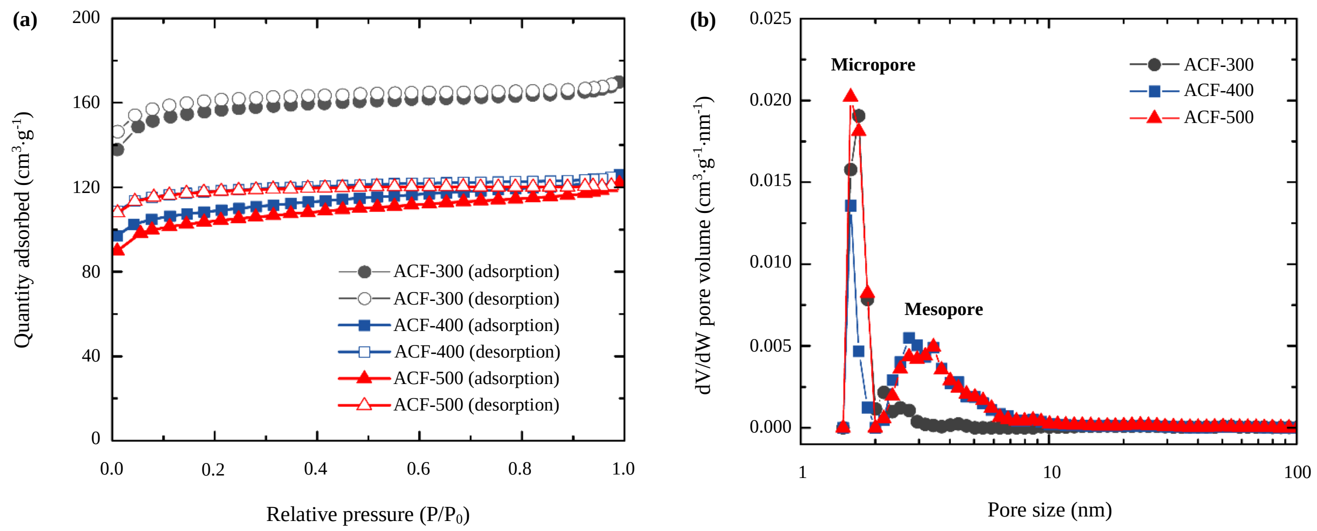

Figure 6. (a) N_2 adsorption-desorption isotherms (the closed and opened symbols represent the adsorption and desorption data, respectively) and (b) DFT pore-size distribution of ACF-300, ACF-400, and ACF-500.

Table 1. Textural parameters determined from N_2 adsorption-desorption isotherms of ACF-300, ACF-400, and ACF-500.

Sample	S_{BET} ($m^2 \cdot g^{-1}$)	S_{micro} ($m^2 \cdot g^{-1}$)	S_{meso} ($m^2 \cdot g^{-1}$)	V_{total} ($cm^3 \cdot g^{-1}$)	V_{micro} ($cm^3 \cdot g^{-1}$)	V_{meso} ($cm^3 \cdot g^{-1}$)	S_{meso}/S_{micro}	V_{meso}/V_{micro}
ACF-300	487	413	74	0.259	0.210	0.049	0.17	0.23
ACF-400	334	271	63	0.192	0.141	0.051	0.23	0.33
ACF-500	326	263	63	0.186	0.133	0.053	0.24	0.40

3.6 Electrochemical measurements

The potential application of ACFs as the electrode materials in supercapacitors was further investigated by the CV and GCD measurements. Figure 7(a) shows the CV curves of ACF-300, ACF-400, and ACF-500 at a scan rate of 20 mV·s^{-1}. All CV curves revealed a quasi-rectangular shape loop with a larger current density at potentials close to 0 V (0 V to 0.4 V) than near 1 V (0.6 V to 1 V). The current bumps at low potentials during the charging stage and the negative current slopes during the discharging stage indicate a pseudo-capacitive behavior due to the presence of oxygen functionality on ACFs [38,39]. The current density from the CV curves was found in the following order: ACF-500 > ACF-400 > ACF-300; this implies improved capacitance at a higher pre-carbonization temperature. Figure 7(b-d) show the CV curves of ACF-300, ACF-400, and ACF-500, respectively, at different scan rates from 10 mV·s^{-1} to 100 mV·s^{-1}. It was evident that the current density of CV loops of all ACFs became larger with a similarly shaped loop at a higher scan rate.

The comparative GCD curves of ACF-300, ACF-400, and ACF-500 within a potential window from 0 V to 1 V at an applied current density of 1 A·g^{-1} are illustrated in Figure 8(a). The GCD curves of all samples showed a non-linear behavior where the slope of the charge and discharge curves (dV/dt) varied with the changing voltage. With the increasing current density, the GCD curves of all ACFs remained in a similar shape with faster charge and discharge times (Figure 8(b-d)). Typically, the specific capacitance (C_p) can be calculated using the slope of the discharge curve in the case that the charge and discharge curves are linear. However, owing to a non-linear GCD curve in this work, the integration of the area under the discharge curve was employed for the calculation of C_p using the following Equation (1) [40]:

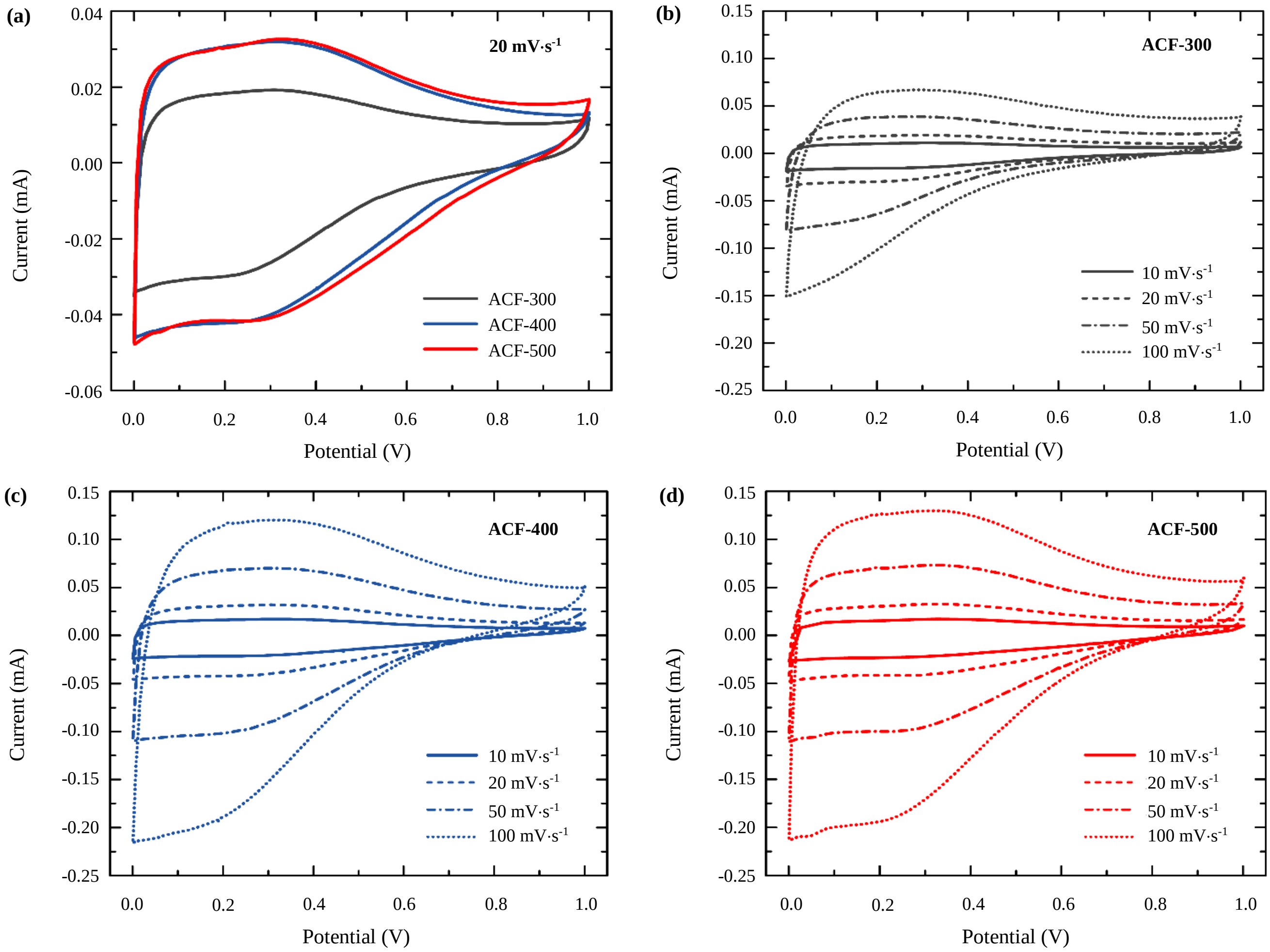

Figure 7. (a) Comparative CV curves of all ACFs at the scan rate of 20 mV·s^{-1}. CV curves at different scan rates (i.e., 10, 20, 50, and 100 mV·s^{-1}) of (b) ACF-300, (c) ACF-400, and (d) ACF-500.

$$C_p = \frac{I}{m}\int \frac{1}{V(t)}dt \qquad (1)$$

where I is the applied constant current (A), m is the mass of active materials (g), and V is the potential as a function of time t (s). The C_p values at a current density of 1 $A{\cdot}g^{-1}$ of ACF-300, ACF-400, and ACF-500 were estimated to be 31.9, 28.8, and 17.5 $F{\cdot}g^{-1}$, respectively. By increasing the current density from 1 to 20 $A{\cdot}g^{-1}$, the C_p value of ACF-300, ACF-400, and ACF-500 decreased to 11.3 $F{\cdot}g^{-1}$, 9.2 $F{\cdot}g^{-1}$, and 4.54 $F{\cdot}g^{-1}$, respectively (Figure 9(a)). A remarkable decrease in the C_p values at a high current density was due to the insufficient time in which electrolyte ions diffused and got arranged inside the pores of ACFs [16,41,42]. ACF-500 was chosen for the stability test by performing 1500 charging and discharging cycles at 5 $A{\cdot}g^{-1}$ (Figure 9(b)). The C_p value of ACF-500 was slightly decreased by about 6% after 1500 cycles, indicating its long-term electrochemical stability.

Furthermore, the relationship between charge storage performance and ACF properties will be discussed based on the aforementioned characterization results. The chemical functional groups and phase structure might be neglected since there were no differences among all ACFs. Therefore, the charge storage performance of ACFs could likely be associated with their surface area and porosity. The C_p value of ACFs was not proportional to the specific surface area as expected but increased with the mesopore to micropore ratios (i.e., $S_{\text{meso}}/S_{\text{micro}}$ and $V_{\text{meso}}/V_{\text{micro}}$). Although a high density of micropores of ACF-300 could result in a high surface area, die-end micropores may inhibit the formation of mass-transport paths and thus reduce the utilization of the active electrode surface. In the case of ACF-400 and ACF-500, which contained both micropores and mesopores, mesopores could create the connection between micropores and also form networked mass-transport channels for high mass-transport rate and low solid-phase resistance for achieving a high C_p value [43-46]. This result indicates that an optimal pore structure with an appropriate mesopore to micropore ratio is a crucial factor, in addition to the surface area, to enhance the C_p value of electrode materials. However, the C_p of ACFs in this work was much more inferior to that of biomass-derived activated carbons reported in the literature due to their small specific surface area and low porosity. The C_p of ACFs could be further improved by enhancing surface area and rationally tailoring the porosity through the increment of the amount of KOH and the adjustment of activation temperature and time.

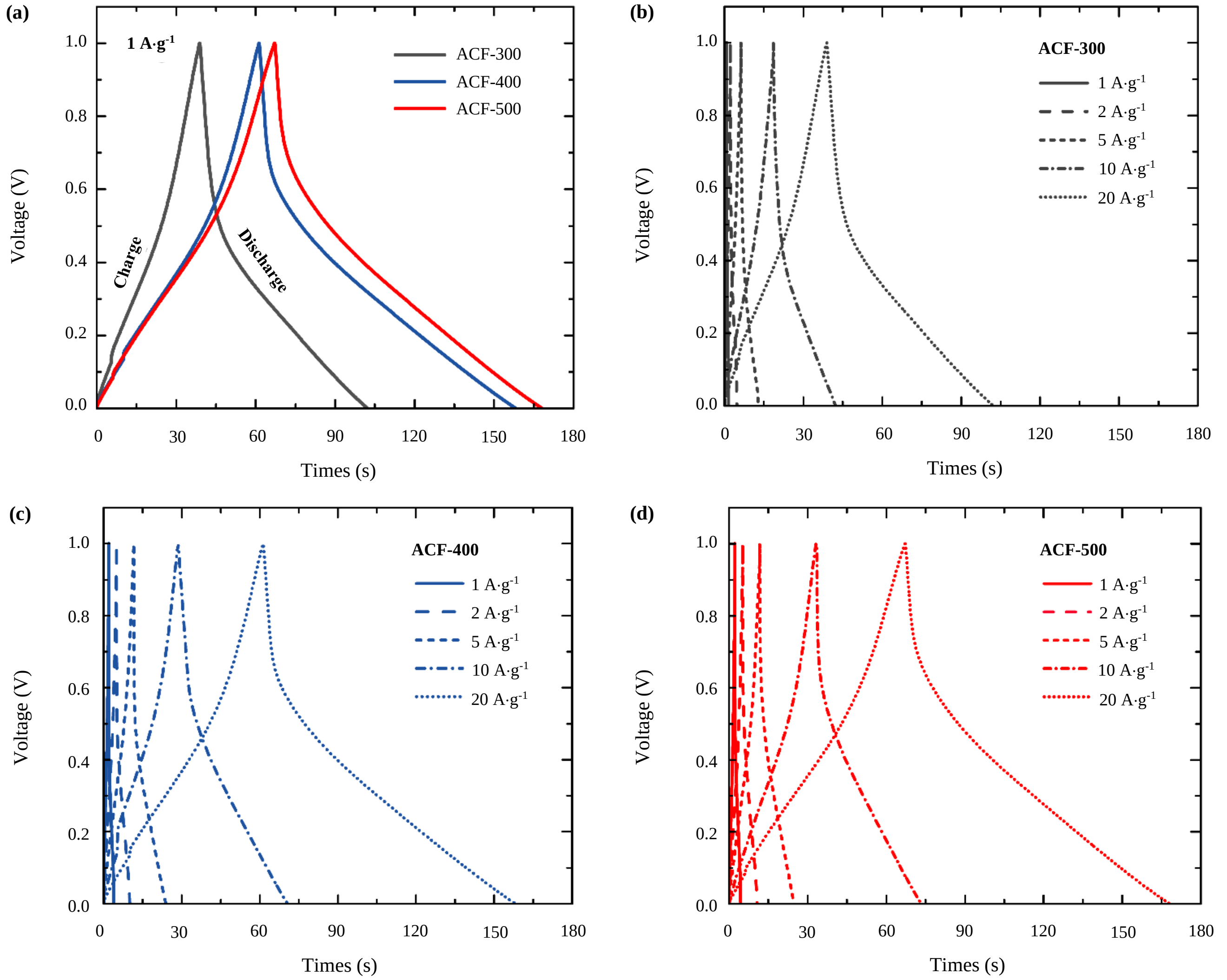

Figure 8. (a) GCD curves of all ACFs at a current density of 1 $A{\cdot}g^{-1}$ within the potential window from 0 V to 1 V. GCD curves at different current densities (i.e., 1, 2, 5, 10, and 20 $A{\cdot}g^{-1}$) of (b) ACF-300, (c) ACF-400, and (d) ACF-500.

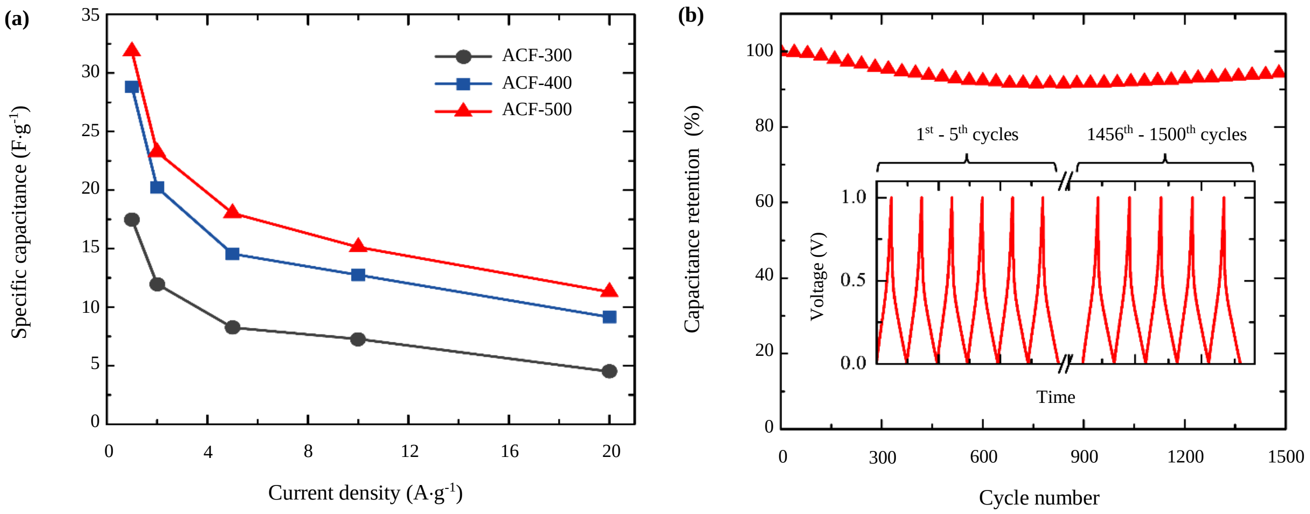

Figure 9. (a) Specific capacitance (C_p) of ACF-300, ACF-400, and ACF-500 at different current densities from 1 A·g^{-1} to 20 A·g^{-1}. (b) Capacitance retention versus cycle number of the ACF-500 measured at 5 A·g^{-1}.

4. Conclusion

Kapok-derived ACFs were successfully synthesized in a two-step process. The kapok was first pre-carbonized at 300°C, 400°C, and 500°C and then subjected to KOH activation at 800°C. The morphological feature of ACFs resembled raw kapok, regardless of their pre-carbonization and activation processes. The ACFs were of an amorphous carbon nature with no impurity phase, as identified by an XRD. By increasing the pre-carbonization temperature, the specific surface area of ACFs decreased, while the mesopore/micropore ratio increased. Despite the lowest specific surface area among all samples, ACF-500 had the highest C_p values (31.9 F·g^{-1} at 1 A·g^{-1}), which was due to its highest mesopore/micropore ratio. This suggests that, in addition to the surface area, the mesopores also play an essential role in enhancing the C_p of ACFs. Although the C_p of ACFs in this work is still inferior to that of other reports, there is a plenty of room for further development and improvement of ACFs to achieve a higher C_p value. The results obtained in this work can be a helpful reference and guideline for further development of ACFs with high surface area and rational pore structure for supercapacitors or related applications.

Acknowledgements

This work was supported by the Kasetsart University Research and Development Institute (KURDI, grant no. FF(KU) 25.64) and International Collaborative Education Program for Material Technology, Education, and Research (ICE-Matter), ASEAN University Network, Southeast Asia Engineering Education Development Network (AUN/SEED-Net), Japan International Cooperation Agency (JICA). The authors would like to thank the International Graduate Student Funding (No. M-2563-02) from the Faculty of Engineering, Kasetsart University.

References

[1] N. Kularatna, "1 - Energy storage devices—a general overview," in Energy Storage Devices for Electronic Systems, N. Kularatna, Ed. Boston: Academic Press, 2015, pp. 1-28.

[2] A. Ter-Gazarian, "Introduction - energy conversion: From primary sources to consumers," in Energy Storage for Power Systems, Institution of Engineering and Technology, pp. 1-4. [Online]. Available: https://app.knovel.com/hotlink/pdf/id:kt00486SA6/energy-storage-power/introduction-energy-conversion

[3] A. González, E. Goikolea, J. A. Barrena, and R. Mysyk, "Review on supercapacitor: Technologies and materials," *Renewable and Sustainable Energy Review*, vol. 58, pp. 1189-1206, 2016.

[4] P. Siwatch, K. Sharma, A. Arora, and S. K. Tripathi, "Review of supercapacitors: Materials and devices," *Journal of Energy Storage*, vol. 21, pp. 801-825, 2019.

[5] S. Liu, L. Wei, and H. Wang, "Review on reliability of supercapacitors in energy storage applications," *Journal of Applied Energy*, vol. 278, p. 115436, 2020.

[6] P. Sharma, and T.S. Bhatti, "A review on electrochemical double-layer capacitors," *Energy Conversion and Management*, vol. 51, pp. 2901-2912, 2010.

[7] S. Fleischmann, J. B. Mitchell, R. Wang, C. Zhan, D. Jiang, V. Presser, and V. Augustyn, "Pseudocapacitance: From fundamental understanding to high power energy storage materials," *Chemical Reviews*, vol. 120, pp. 6738-6782,

[8] D. P. Chatterjee, and A. K. Nandi, "A review on the recent advances in hybrid supercapacitors," *Journal of Materials Chemistry A*, vol. 9, pp. 15880-15918, 2021.

[9] Z. Bi, Q. Kong, Y. Cao, G. Sun, F. Su, X. Wei, X. Li, A. Ahmad, L. Xie, and C.-M. Chen, "Biomass-derived porous carbon materials with different dimensions for supercapacitor electrodes: a review," *Journal of Materials Chemistry A*, vol. 7, pp. 16028-17045, 2019.

[10] Y. Wang, Q. Qu, S. Gao, G. Tang, K. Liu, S. He, and C. Huang, "Biomass derived carbon as binder-free electrode materials for supercapacitors," *Carbon*, vol. 155, pp. 706-726, 2019.

[11] S. Saini, P. Chand, and A. Joshi, "Biomass derived carbon for supercapacitor applications: Review," *Journal of Energy Storage*, vol. 39, p. 10246, 2021.

[12] Y. J. Kim, Y. Abe, T. Yanagiura, K. C. Park, M. Shimizu, T. Iwazaki, S. Nakagawa, M. Endo, and M. S. Dresselhaus,

"Easy preparation of nitrogen-enriched carbon materials from peptides of silk fibroins and their use to produce a high volumetric energy density in supercapacitors," *Carbon*, vol. 45, pp. 2116-2125, 2007.

[13] Y. Liu, Z. Shi, Y. Gao, W. An, Z. Cao, and J. Liu, "Biomass-swelling assisted synthesis of hierarchical porous carbon fibers for supercapacitor electrodes," *ACS Applied Materials Interfaces*, vol. 8, pp. 28283-28290, 2016.

[14] P. Cheng, T. Li, H. Yu, L. Zhi, Z. Liu, and Z. Lei, "Biomass-derived carbon fiber aerogel as a binder-free electrode for high-rate supercapacitors," *The Journal of Physical Chemistry C*, vol. 120, pp. 2079-2086, 2016.

[15] X.-L. Su, S. Jiang, G.-P. Zheng, X.-C. Zheng, J.-H. Yang, and Z.-Y. Liu, "High-performance supercapacitors based on porous activated carbons from cattail wool," *Journal of Materials Science*, vol. 53, pp. 9191-9205, 2018.

[16] M. Li, H. Xiao, T. Zhang, Q. Li, and Y. Zhao, "Activated carbon fiber derived from sisal with large specific surface area for high-performance supercapacitors," *ACS Sustainable Chemistry Engineering*, vol. 7, pp. 4716-4723, 2019.

[17] J.-T. Chung, K.-J. Hwang, W.-G. Shim, C. Kim, J.-Y. Park, D.-Y. Choi, and J.-W. Lee, Synthesis and characterization of activated hollow carbon fibers from *Ceiba pentandra (L.) Gaertn.* (kapok)," *Materials Letters*, vol. 93, pp. 401-403, 2013.

[18] Y. Cao, L. Xie, G. Sun, F. Su, Q.-Q. Kong, F. Li, W. Ma, J Shi, D. Jiang, C. Lu, and C.-M. Chen, "Hollow carbon microtubes from kapok fiber: structural evolution and energy storage performance," *Sustainable Energy & Fuels*, vol. 2, pp. 455-465, 2018.

[19] V. Subramanian, C. Luo, A. M. Stephan, K. S. Nahm, S. Thomas, and B. Wei, "Supercapacitors from activated carbon derived from banana fibers," *The Journal of Physical Chemistry C*, vol. 111, pp. 7527-7531, 2007.

[20] A. Linares-Solano, and D. Cazorla-Amorós, "Activated Carbon Fibers," in Handbook of Advanced Ceramics, Elsevier, 2013, pp. 155-169.

[21] J. Phiri, J. Dou, T. Vuorinen, P. A. C. Gane, and T. C. Maloney, "Highly porous willow wood-derived activated carbon for high-performance supercapacitor electrodes," *ACS Omega*, vol. 4, pp. 18108-18117, 2019.

[22] S.-X. Liang, F.-F. Duan, Q.-F. Liu, and H. Yang, "Hierarchical biocarbons with controlled micropores and mesopores derived from kapok fruit peels for high-performance supercapacitor electrodes," *ACS Omega*, vol. 4, pp. 5991-5999, 2019.

[23] X. Bai, Z. Wang, J. Luo, W. Wu, Y. Laing, X. Tong, and Z. Zhao, "Hierarchical porous carbon with interconnected ordered pores from biowaste for high-performance supercapacitor electrodes," *Nanoscale Research Letters*, vol. 15, p. 88, 2020.

[24] K. Hina, H. Zou, W. Qian, D. Zuo, and C. Yi, "Preparation and performance comparison of cellulose-based activated carbon fibres," *Cellulose*, vol. 140, pp. 465-476, 2018.

[25] H. Yang, R. Yan, H. Chen, D. Ho.Lee, and C. Zheng, "Characteristics of hemicellulose, cellulose and lignin pyrolysis," *Fuel*, vol. 86, pp. 1781-1788, 2007.

[26] C. L. Waters, R. R. Janupala, R. G.Mallinson, and L. L. Lobban, "Staged thermal fractionation for segregation of lignin and cellulose pyrolysis products: An experimental study of residence time and temperature effects," *Journal of Analytical and Applied Pyrolysis*, vol. 126, pp. 380-389, 2017.

[27] Q. Tian, X. Wang, X. Xu, M. Zhang, L. Wang, X. Zhao, Z. An, H. Yao, and J. Gao, "A novel porous carbon material made from wild rice stem and its application in supercapacitors," *Materials Chemistry Physics*, vol. 213, pp. 267-276, 2018.

[28] S. F. S. Draman, R. Daik, F. A. Latif, and S. M. El-Sheikh, "Characterization and thermal decomposition kinetics of kapok (*Ceiba pentandra L.*)–based cellulose," *Bioresources*, vol. 9, pp. 8-23, 2014.

[29] N. Paksung, J. Pfersich, P. J. Arauzo, D. Jung, and A. Kruse, "Structural effects of cellulose on hydrolysis and carbonization behavior during hydrothermal treatment," ACS Omega, vol. 51, pp. 12210-12223, 2020.

[30] L. Qin, Z. Hou, S. Zhang, W. Zhang, and E. Jiang, "Super-capacitive charge storage properties of porous carbons derived from pine nut shells," *Journal of Electroanalysis Chemistry*, vol. 866, p. 114140, 2020.

[31] L. Chunlan, X. Shaoping, G. Yixiong, L. Shuqin, and L. Changhou, "Effect of pre-carbonization of petroleum cokes on chemical activation process with KOH," *Carbon*, vol. 43, no. 11, pp. 2295-2301, 2005.

[32] E. Jang, S. W. Choi, and K. B. Lee, "Effect of carbonization temperature on the physical properties and CO_2 adsorption behavior of petroleum coke-derived porous carbon," *Fuel*, vol. 248, pp. 85-92, 2019.

[33] J. Deng, T. Xiong, H. Wang, A. Zheng, and Y. Wang, "Effects of cellulose, hemicellulose, and lignin on the structure and morphology of porous carbons," *ACS Sustainable Chemistry Engineering*, vol. 4, pp. 3750-3756, 2016.

[34] K. S. W. Sing, D. H. Everett, E. A. W. Haul, L. Moscou, R. A. Pierotti, J. Rouquérol, and T. Siemieniewska, "Reporting physisorption data for gas/solid systems with special reference to the determination of surface area and porosity," *Pure Applied Chemistry*, vol. 57, pp. 603-619, 1985.

[35] K. S. W. Sing, and R. T. Williams, "Physisorption hysteresis loops and the characterization of nanoporous materials," *Adsorption Science and Technology*, vol. 22, pp. 733-782, 2004.

[36] W. Lai, S. Yang, Y. Jiang, F. Zhao, Z. Li, B. Zaman, M. Fayaz, X. Li, and Y. Chen, "Artefact peaks of pore size distributions caused by unclosed sorption isotherm and tensile strength effect," *Adsorption*, Vol. 26, pp. 633-644, 2020.

[37] R. Ojeda-López, G. Ramos-Sánchez, C. García-Mendoza, D. C. S. Azevedo, A. Guzmán-Vagas, and C. Felipe, "Effect of calcination temperature and chemical composition of PAN-derived carbon microfibers on N_2, CO_2, and CH_4 adsorption," *Materials*, vol .14, no. 14, pp. 3914, 2021.

[38] P. Zhang, S. Xie, Y. Qiu, Y. Jiao, C. ji, Y. Li, H. Fan, and X. Li, "Facile preparation of porous carbon nanomaterials for robust supercapacitors," *Journal of Materials Research*, vol. 33, pp. 1142-1154, 2018.

[39] A. Saning, S. Herou, D. Dechtrirat, C. Ieosakulrat, P. Pakawatpanurut, S. Kaowphong, C. Thanachayanont, M.-M. Titirici, and L. Chuenchom, "Green and sustainable zero-waste conversion of water hyacinth (Eichhornia crassipes) into superior

magnetic carbon composite adsorbents and supercapacitor electrodes," *RSC Advances*, vol. 9, 24248-24258, 2019.

[40] T. S. Mathis, N. Kurra, X. Wang, D. Pinto, P. Simon, and Y. Gogotsi, "Energy storage data reporting in perspective – Guidelines for interpreting the performance of electrochemical energy storage systems", *Advanced Energy Materials*, vol. 9, p. 1902007, 2019.

[41] C. Wei, J. Yu, X. Yang, and G. Zhang, "Activated carbon fibers with hierarchical nanostructure derived from waste cotton gloves as high-performance electrodes for supercapacitors," *Nanoscale Research Letters*, vol. 12, p. 379, 2017.

[42] L.-H. Zheng, M.-H. Chen, Shu-Xia Liang, and Q-F Lü, Oxygen-rich hierarchical porous carbon derived from biomass waste-kapok flower for supercapacitor electrode," *Diamond and Related Materials*, vol. 113, p. 108267, 2021.

[43] Y. Lu, S. Zhang, J. Yin, C. Bai, J. Zhang, Y. Li, Y. Yang, Z. Ge, L. Wei, M. ma, Y. Ma, and Y. Chen, "Mesoporous activated carbon materials with ultrahigh mesopore volume and effective specific surface area for high performance supercapacitors," *Carbon*, vol. 124, pp. 64-71, 2017.

[44] J. Yang, H. Wu, M. Zhu, W. Ren, Y. Lin, H. Chen, and F. Pan, "Optimized mesopores enabling enhanced rate performance in novel ultrahigh surface area meso-/microporous carbon for supercapacitors," *Nano Energy*, vol. 33, pp. 453-461, 2017.

[45] S. Herou, M. C. Ribadeneyra, R. Madhu, V. Araullo-Peters, A. Jensen, P.Schlee, and M. Titirici, "Ordered mesoporous carbons from lignin: a new class of biobased electrodes for supercapacitors," *Green Chemistry*, vol. 21, pp. 550-559, 2019.

[46] Y. Zhang, C. Wu, S. Dai, L. Liu, H. Zhang, W. Shen, W. Sun, and C. M. Li, "Rationally tuning ratio of micro- to meso-pores of biomass-derived ultrathin carbon sheets toward supercapacitors with high energy and high power density," *Journal of Colloid and Interface Science*, vol. 600, pp. 817-825, 2022.